High energy neutrino yields from astrophysical sources. II. Magnetized sources

M. Kachelrieß,[1] S. Ostapchenko,[2,3] and R. Tomàs[4]

[1]*Institutt for fysikk, NTNU, N-7491 Trondheim, Norway*
[2]*Institut für Experimentelle Kernphysik, Universität Karlsruhe, 76021 Karlsruhe, Germany*
[3]*D. V. Skobeltsyn Institute of Nuclear Physics, Moscow State University, 119992 Moscow, Russia*
[4]*AHEP Group, Institut de Física Corpuscular–C.S.I.C./Universitat de València, Edifici Instituts d'Investigació,
Apartado 22085, E-46071 València, Spain*

We calculate the yield of high energy neutrinos produced in astrophysical sources for arbitrary interaction depths τ_0 and magnetic field strengths B. We take into account energy loss processes like synchrotron radiation and diffusion of charged particles in turbulent magnetic fields as well as the scattering of secondaries on background photons and the direct production of charm neutrinos. Meson-photon interactions are simulated with an extended version of the SOPHIA model. Diffusion leads to an increased path length before protons leave the source of size R_s and therefore magnetized sources lose their transparency below the energy $E \sim 10^{18}$ eV$(R_s/\text{pc})(B/\text{mG})\tau_0^{1/\alpha}$, with $\alpha = 1/3$ and 1 for Kolmogorov and Bohm diffusion, respectively. Moreover, the neutrino flux is suppressed above the energy where synchrotron energy losses become important for charged particles. As a consequence, the energy spectrum and the flavor composition of neutrinos are strongly modified both at low and high energies even for sources with $\tau_0 \lesssim 1$.

PACS numbers: 95.85.Ry, 14.60.Lm, 14.60.Pq, 98.70.Sa

I. INTRODUCTION

High energy neutrinos from astrophysical sources are the decay products of secondary mesons produced by scattered high energy protons on background protons or photons. A classic example are the so-called cosmogenic or Greisen-Zatsepin-Kuzmin neutrinos produced in scatterings of extragalactic ultrahigh energy cosmic rays on cosmic microwave photons during propagation [1]. Since the sources of ultrahigh energy cosmic rays unavoidably contain also matter and photons, all cosmic ray sources like active galactic nuclei (AGN) or gamma-ray bursts should produce to some extent also high energy neutrinos [2–5]. However, the elusive nature of their interactions has prevented so far the detection of neutrinos from sources other than the Sun and SN1987A, despite intensive experimental efforts.

Theoretical limits or predictions for neutrino fluxes are therefore important as a guideline for experimentalists. Two different kinds of bounds on high energy neutrino fluxes exist: The cascade or EGRET limit uses bounds on the diffuse MeV-GeV photon background to limit the energy transferred to electromagnetically interacting particles that are produced unavoidably together with neutrinos [6]. The cosmic ray upper bounds of, e.g., Refs. [7,8] use the observed ultrahigh energy cosmic ray flux to restrict possible neutrino fluxes. One of the several underlying assumptions of the latter limit is that all neutrino sources are transparent to hadronic interactions and thus at least neutrons can escape from the source region without interactions.

In a previous work, we calculated the flux of high energy neutrinos produced as secondaries in astrophysical sources with arbitrary interaction depth but negligible magnetic fields [9]. The present work extends Ref. [9] in two respects: First, multiple interactions that become relevant in a thick source require the modeling not only of photonucleon ($N + \gamma \longrightarrow X$), but also of photomeson ($\pi + \gamma \longrightarrow X$, $K + \gamma \longrightarrow X$) interactions. The latter are treated now within a self-consistent extension of the SOPHIA model [10]. Second, and more importantly, we have added the effects of possible magnetic fields around the source region. This includes diffusion of charged particles in turbulent magnetic fields and energy loss processes like synchrotron radiation. As a result, the shape of the neutrino spectra deviates strongly from the injection spectrum of protons even for transparent sources, $\tau_0 \lesssim 1$, both at the low and the high energy end of the produced neutrino flux. Moreover, the relative importance of the various channels contributing to the neutrino yields changes strongly, leading thereby to large variations in the neutrino flavor composition as a function of the energy. Specific examples are the cases where the neutrino spectrum is dominated by kaon decays [11,12] or influenced by muon damping [13].

We restrict ourselves to describe the neutrino sources by a schematic toy model, assuming e.g. a constant magnetic field strength throughout the source, in order to illustrate in the most transparent way these phenomena. The application of our simulation to concrete astrophysical models and a comparison with earlier studies of neutrino fluxes from AGN cores [3] and jets [4], clusters of galaxy [14], or hidden sources [15] will be performed in paper III of this series [16].

The present work is structured as follows: In Sec. II, we discuss how we simulate the interactions and the propagation of charged particles. In particular, we describe our extension of the SOPHIA model, the continuous energy loss

processes considered, and how we account for diffusion. In Sec. III, we discuss the influence of magnetic fields on the escaping proton flux. Armed with our understanding of the proton fluxes, we continue in Sec. IV to examine the resulting neutrino fluxes and in Sec. V their flavor composition. Finally, we summarize our results in Sec. VI.

II. SIMULATION OF PARTICLE INTERACTIONS AND PROPAGATION

A. Simulation of photon-hadron interactions

The SOPHIA model [10] was designed by Mücke *et al.* to treat gamma-nucleon interactions in the broad energy range from the production threshold of mesons up to TeV center of mass (c.m.) energies $\sqrt{s}$. The underlying physics is described in Ref. [10]. We have performed a direct generalization of the SOPHIA approach for the case of gamma-meson ($\pi^\pm$, $K^\pm$, K_0, $\bar{K}_0$) interactions. As in the γN case, the dominant mechanisms are resonance production and binary processes at low energies and Reggeon (Pomeron) exchanges at high ones. We have included the known resonances, with well measured e/m branching width, from the compilation in the Review of Particle Properties [17]. All the resonances were assumed to decay isotropically. Concerning the direct meson production, the only difference compared to the γN case is that the virtual meson-nucleon coupling is replaced by the meson-meson one, as shown in Fig. 1.

In the energy range of interest, experimental data on binary processes in hadron-hadron and gamma-hadron collisions are in a very good agreement with the additive quark model (AQM) predictions [18]. Thus, we define the meson-hadron coupling as the sum of the contributions corresponding to the coupling to "dressed" constituent quarks. Correspondingly, for the cross section for the binary process $\gamma\pi^\pm \to \pi^\pm\pi^0$ we use the SOPHIA parametrization for the reaction $\gamma p \to \pi^+ n$ (with properly modified hadron production threshold), based on the fact that the number of valence (anti)quarks in the pion is the same as the number of valence u-quarks in the proton. The same parametrization is used for $\gamma K^+ \to \pi^+ K_0$ (similarly for other kaons), now being rescaled by a factor 1/2, corresponding to having just one light valence (anti)quark in kaons. Here we neglect the t-channel exchange of kaon
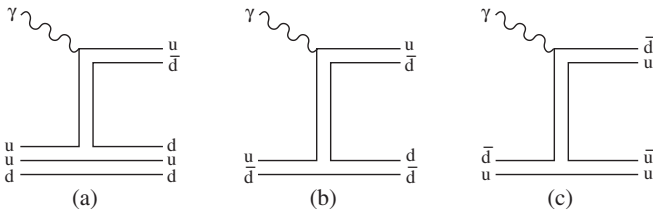
states, which is mass squared suppressed compared to pion exchange.

A remarkable property of Reggeon exchanges is the factorized form of the corresponding amplitude, which is parametrized as [19]

$$A_{ab}^{\mathbb{R}^\zeta}(s,t) = 8\pi s_0 g_a^{\mathbb{R}^\zeta}(t) g_b^{\mathbb{R}^\zeta}(t) \eta_{\mathbb{R}^\zeta}(t) \left(\frac{s}{s_0}\right)^{\alpha_{\mathbb{R}^\zeta}(t)} \quad (1)$$

$$\eta_{\mathbb{R}^\zeta}(t) = \frac{1 + \zeta \exp(-i\pi\alpha_{\mathbb{R}^\zeta}(t))}{\sin(-i\pi\alpha_{\mathbb{R}^\zeta}(t))}, \quad (2)$$

where $\alpha_{\mathbb{R}^\zeta}(t)$ is the Regge trajectory for the Reggeon $\mathbb{R}^\zeta$, $g_a^{\mathbb{R}^\zeta}(t)$ the Reggeon-hadron a vertex, and $\zeta = \pm 1$ is the Reggeon signature; $s_0 \simeq 1$ GeV^2 is the hadronic mass scale. This expression is also valid for Pomeron exchange, the latter being a particular Reggeon case, corresponding to the intercept $\alpha_{\mathbb{P}}(0) > 1$, positive signature, and zero transfer of quantum numbers. This allowed to construct very successful parametrizations for high energy behavior of hadron-hadron and gamma-proton cross sections [20], which include only three terms: exchanges of Reggeons with positive ($\mathbb{R}^+$) and negative ($\mathbb{R}^-$) signature, and of the Pomeron ($\mathbb{P}$)

$$\sigma_{ab}(s) = C_{ab}^{\mathbb{R}^+} s^{\alpha_{\mathbb{R}^+}(0)-1} + C_{ab}^{\mathbb{R}^-} s^{\alpha_{\mathbb{R}^-}(0)-1} + C_{ab}^{\mathbb{P}} s^{\alpha_{\mathbb{P}}(0)-1}, \quad (3)$$

where the constants C_{ab}^X are related to the Reggeon and Pomeron couplings to hadrons a and b, $C_{ab}^X \sim g_a^X(0) g_b^X(0)$, and the energy exponents of the three terms in (3) are expressed via the intercepts $\alpha_X(0)$ of the corresponding Regge trajectories and do not depend on the types of interacting hadrons. Thus, we can obtain the corresponding parameters for $\gamma\pi$ and γK interactions as

$$C_{\gamma\pi}^X = C_{\gamma p}^X \frac{C_{\pi^+ p}^X}{C_{pp}^X} \quad (4)$$

$$C_{\gamma K}^X = C_{\gamma p}^X \frac{C_{K^+ p}^X}{C_{pp}^X}, \quad (5)$$

for $X = \mathbb{R}^+$, $\mathbb{P}$. On the other hand, we have $C_{\gamma h}^{\mathbb{R}^-} = 0$, as the Reggeons with negative signature do not contribute to γh scattering. The parameters $C_{\gamma p}^X$, C_{hp}^X, $\alpha_X(0)$ have been taken from the same cross section fits [17] which have been already employed in the SOPHIA model.

The calculated total $\gamma\pi$ and γK cross sections, as well as partial contributions of various interaction channels, are plotted in Figs. 2–4.

In contrast to the γN case [10], production of resonances does not play a very prominent role in $\gamma\pi$ and γK collisions, because of the comparatively high energy thresholds of these processes. On the other hand, of considerable importance is the direct pion production, which starts already at the hadron production threshold. It is worth stressing again that both the direct contribution and the one of Reggeon and Pomeron exchanges, dominant at high energies, are well defined by the proper rescaling from the γN
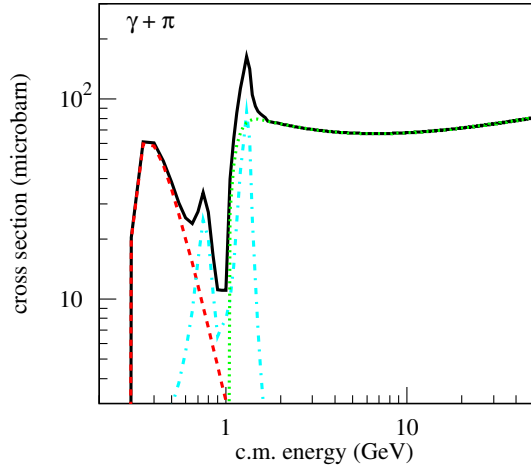

FIG. 1. Direct π^+ production in γp (a) and $\gamma\pi^+$ (b), (c) interactions.

FIG. 2 (color online). The $\gamma\pi^{\pm}$ total cross section (solid line) and the contributions of the direct process (dashed line), of resonance production (dot-dashed lines) and of Reggeon and Pomeron exchanges (dotted line).

case; the former using the AQM picture, the latter within the Regge theory framework.

For particle production, like in the original SOPHIA, we used the Lund JETSET 7.4 string fragmentation procedure [21], as well as SOPHIA's original distribution for the energy-momentum partition between valence constituents. Also, we have kept the same proportion between diffractive and nondiffractive final states for $\gamma\pi$ and γK interactions as the one for the γp case in SOPHIA.[1] In summary, the described generalization of the SOPHIA interaction mechanism for $\gamma\pi$ and γK collisions is well defined: All the relevant parameters are fixed either by experimental data or by theoretical arguments. Finally, we note that, in comparison with the simplified modeling of pion and kaon interactions in Ref. [9], the interaction lengths of pions and kaons are reduced outside the resonance region by $\sim 35\%$.

B. Interactions in the continuous energy loss approximation

The following interactions are treated in the continuous energy loss approximation.

(1) Synchrotron radiation: Processes in external magnetic fields are characterized by the parameters $\chi = eF_{\mu\nu}p^\mu p^\nu/m^3 = (p_\perp/m)(B/B_{cr})$ and $B_{cr} = m^2/e$. The intensity of synchrotron radiation can be approximated for $B \ll B_{cr}$ by [22]

$$\frac{W}{W_{cl}} = 1 - \frac{55\sqrt{3}}{24}\xi + \frac{64}{3}\xi^2 + \cdots, \qquad \xi \ll 1,$$
$$= 2^{8/3}\Gamma(2/3)\xi^{-4/3} + \cdots, \qquad \xi \gg 1, \qquad (6)$$

---

[1]One may expect some difference in the diffraction excitation probability for pions and kaons compared to protons. The data on pp, πp, and Kp interactions indicate that this difference is at the 10% level and therefore is inessential for our applications.
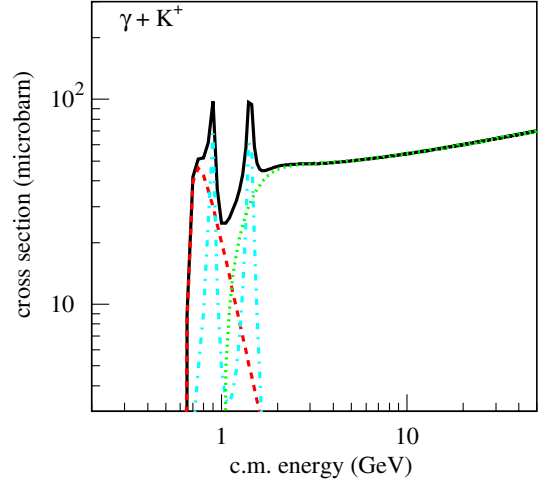

FIG. 3 (color online). The $\gamma K^{\pm}$ total cross section and the contributions of various interaction channels. The abbreviations for the curves are the same as in Fig. 2.

where $\xi = 2\chi/3$ and $W_{cl} = (2/3)\alpha m^2\chi^2$ is the classical intensity of synchrotron radiation. We glue the two approximations at $\xi = 0.8$ together. The energy loss per time is $\beta = dE/dt = -W$. We define as typical length scale l_{syn} of synchrotron losses (in the classical limit $\xi \ll 1$)

$$l_{syn} = \left(\frac{1}{E}\frac{dE}{dt}\right)^{-1} = \frac{3}{2\alpha m}\frac{1}{\gamma}\left(\frac{B_{cr}}{B}\right)^2. \qquad (7)$$

(2) Below the pion-production threshold, e^+e^- pair production on photons becomes for low magnetic field strengths the main energy loss mechanism of charged hadrons. We use the energy losses as calculated in Ref. [23].
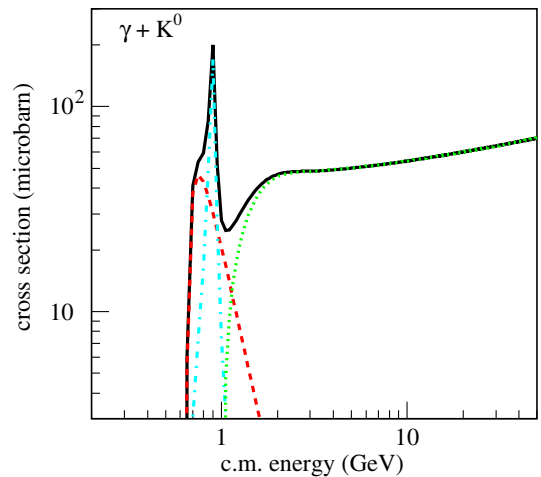

FIG. 4 (color online). The γK_0 total cross section and the contributions of various interaction channels. The abbreviations for the curves are the same as in Fig. 2.

(3) For muons, we include energy losses due to inverse Compton scattering from Ref. [24].

In the following, we will consider static sources and neglect the possible effects of adiabatic cooling as well as the energy losses due to curvature radiation. The latter is formally equivalent to synchrotron radiation after the replacement of the Larmor radius $R_L = E/(eB)$ with the curvature radius R_C and needs therefore no special consideration.

C. Diffusion in magnetic fields

The magnetic fields present in the surrounding of the acceleration region induce not only synchrotron radiation as an important energy loss process discussed in the previous subsection, but lead also to deviations from straight-line propagation for charged particles. The transition between the ballistic and the diffusion regime happens approximately at the energy E_L when the Larmor radius,

$$R_L = 1.08 \times 10^{-3} \text{ pc} \frac{E}{10^{18} \text{ eV}} \frac{\text{G}}{B}, \qquad (8)$$

equals the source size R_s, i.e. at the energy

$$E_L = 10^{18} \text{ eV}(R_s/\text{pc})(B/\text{mG}). \qquad (9)$$

In a turbulent magnetic field, the path of a charged particle can be modeled either as a random walk from a microscopic or as a diffusion process from a macroscopic point of view. We shall use the latter picture and need to specify thus the energy-dependent diffusion coefficient $D(E)$. Following Ref. [25], we use

$$D(E) = D_0\left[\left(\frac{R_L}{l_c}\right)^a + \left(\frac{R_L}{l_c}\right)^2\right] \quad \text{for } E < E_L, \qquad (10)$$

where l_c denotes the coherence length of the magnetic field and $a = 1/3$ and 1 correspond to the case of Kolmogorov and Bohm diffusion, respectively [26].

The diffusion time t_{diff} is defined as the typical time a charged particle needs to diffuse the distance R_s assuming negligible energy losses,

$$t_{\text{diff}} = \frac{R_s^2}{6D}. \qquad (11)$$

Thus, the effective size R_{eff} of a magnetized source becomes $R_{\text{eff}} = t_{\text{diff}} = R_s^2/(6D)$. We choose the normalization constant D_0 in Eq. (10) such that the effective source size equals the true one, $R_{\text{eff}} = R_s$, for E_L,

$$D_0 = \frac{R_s}{6}\left(\frac{l_c}{R_s}\right)^2 \frac{1}{1 + (l_c/R_s)^{2-a}}. \qquad (12)$$

Without diffusion, one defines the interaction depth as the ratio $\tau_0 = R_s/l_{\text{int}}$ of the source size R_s to the interaction length l_{int} of nucleons with photons. For the illustration of our numerical results, we determine in the following τ_0 via $l_{\text{int}} = 1/(n_\gamma\sigma)$ with $\sigma = 0.2$ mb above the threshold E_{th} as reference cross section. Therefore in the case of a

background of thermal photons with temperature T, the interaction length becomes $l_{\text{int}} \approx 2.5 \times 10^{26}(T/\text{K})^{-3}$ cm. In the case of diffusion, it is convenient to introduce additionally an effective interaction depth $\tau_{\text{eff}} = R_{\text{eff}}/l_{\text{int}}$ or

$$\tau_{\text{eff}} = \begin{cases} \tau_0 & \text{for } E \geq E_L \\ \tau_0(\frac{E_L}{E})^a \frac{1+(R_s/l_c)^{2-a}}{1+(R_L/l_c)^{2-a}} & \text{for } E < E_L. \end{cases} \qquad (13)$$

Thus, a source that is transparent at high energies, when particles move in the ballistic regime, becomes thick in the diffusion regime below the energy $\sim E_L\tau_0^{1/a}$.

D. Summary of interactions and propagation

We idealize a neutrino source as an acceleration region surrounded by a sphere of radius R_s containing photons and turbulent magnetic fields. The photon energy distribution may follow either a (broken) power law or a thermal Planck spectrum, although here we present results in most cases only for a Planck distribution. The probability $\mathcal{N}$ that a particle diffuses outwards the distance Δr without scattering or decay is given by

$$\mathcal{N} = \exp\left(-\int_r^{r+\Delta r} dl(l_{\text{dec}}^{-1} + l_{\text{int}}^{-1})\right), \qquad (14)$$

where l_{dec} and l_{int} are its decay and interaction length, respectively.[2] The path length Δl of the trajectory and the distance Δr diffused outwards are connected by

$$\nu(E) = \frac{\Delta l}{\Delta r} = \frac{R_s}{6D}. \qquad (15)$$

Thus, diffusion enhances interactions and energy losses by the factor $\nu(E) \propto 1/D(E)$ for $E \leq E_L$. The energy of the particle along the path l is obtained by integrating the energy losses $\beta(E)$. Note that in the calculation of diffusion coefficients one assumes generally negligible energy losses. Thus, Eq. (15) neglects the decrease of the diffusion coefficient along the particle trajectory and hence underestimates the interaction depth and the true number of interactions.

In our Monte Carlo simulation, we track explicitly all secondaries (N, $\pi^\pm$, $K^\pm$, $K_{L,S}^0$) for which the interaction rate is non-negligible compared to their decay rate, and take into account the possibility to produce prompt charm neutrinos; for details see [9].

III. PROTON FLUX

For the illustration of our results we have chosen in the following always for the initial proton flux a power-law dependence, $dN_p/dE = KE^{-\alpha_g}$ with $\alpha_g = 2$, and a rather high value of the maximal energy $E_{\text{max}} = 10^{24}$ eV. In order to facilitate the comparison with our previous

---

[2]The corresponding equation in Ref. [9] contains a typographical error.

work, Ref. [9], we consider only thermal distributions of background photons.

Sources with negligible magnetic fields were thoroughly discussed in Ref. [9]. While in this case the initial and final proton fluxes deviate strongly for thick sources, they basically coincide for transparent ones. By contrast, the final proton spectrum is strongly distorted even for a transparent source, if the magnetic field in the source is sufficiently large: At high energies, synchrotron radiation losses lead to a change in the spectral index of the final proton flux, while at low enough energies protons start to diffuse in the turbulent magnetic field. Thereby the number of interactions increases, the proton flux is suppressed, and at the same time the production of neutrons is enhanced. As we will show now, the cosmic ray flux from a magnetized source has bumps and breaks, and may even suddenly decrease by orders of magnitude.

A. Low energy protons and diffusion

We start our analysis by studying the consequences of diffusion on the final proton flux. In Fig. 5, we show the effective size $R_{\rm eff}$ of a thin source with $T = 10^4$ K, $R_s = 2.5 \times 10^{13}$ cm ($\tau_0 = 0.1$) and a magnetic field strength $B = 100$ G for various different diffusion regimes: The case of a magnetic field coherent over the entire source, $l_c = R_s$, is shown for Bohm diffusion, $a = 1$, as a black solid and for Kolmogorov diffusion, $a = 1/3$, as a red solid line, respectively. Additionally, $R_{\rm eff}$ is shown for $a = 1$ and $l_c = 10^{-2}R_s$ as a blue solid line and compared to other typical length scale as the interaction length, the Larmor
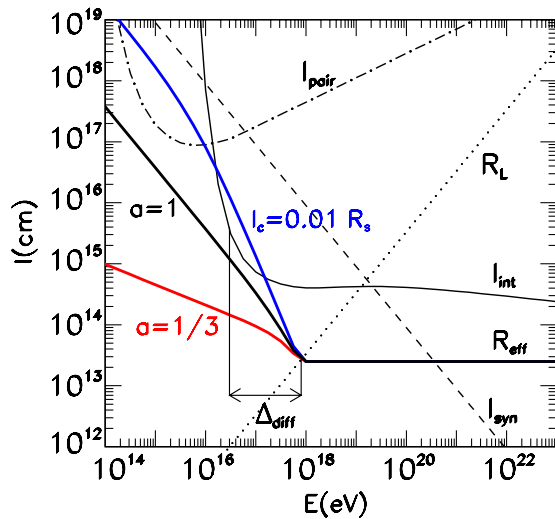

FIG. 5 (color online). Effective size (thick solid) of a source with a temperature of $T = 10^4$ K, size $R_s = 2.5 \times 10^{13}$ cm ($\tau_0 = 0.1$), and magnetic field $B = 100$ G for $a = 1$ (black), $a = 1/3$ (red), and with $l_c = 10^{-2}R_s$ and $a = 1$ (blue). The interaction length (thin solid), the Larmor radius (dotted), and the typical length scale of energy losses from synchrotron radiation (dashed) and e^+e^- pair production (dot-dashed) in the case of protons are also shown.

radius (dotted), and the synchrotron losses (dashed) for protons. The behavior of $R_{\rm eff}$ is the expected one: Protons with $E > E_L \approx 8 \times 10^{17}$ eV propagate approximately on straight lines, and thus $R_{\rm eff} = R_s$. At lower energies, protons start to diffuse and $R_{\rm eff}$ increases. The steepness of this increase depends on the energy dependence of the diffusion coefficient $D(E)$, i.e. on a and the value of the coherence length l_c. For $R_L(E) \lesssim l_c$, the effective size is proportional to E^{-a}. If the coherence length turns out to be smaller than R_s, then $R_{\rm eff}$ is proportional to E^{-2} in the energy range from E_L down to the energy where $R_L(E) = l_c$. In this case the effect of diffusion is strongest, see Fig. 5.

The increase of $R_{\rm eff}$ implies a change in the final proton flux, only if E_L is larger than the threshold energy $E_{\rm th}$ for photopion production. In Fig. 5, we show the width $\Delta_{\rm diff} \equiv \log(E_L) - \log(E_{\rm th})$ assuming $E_{\rm th} = m_p m_\pi/(2\varepsilon_\gamma)$, with $\varepsilon_\gamma = 2.7T$. Inside this window, even a transparent source can become opaque, as it is illustrated by the increase of the effective interaction depth $\tau_{\rm eff}$ shown in Fig. 6 in the case of diffusion.

The impact of a change of $\tau_{\rm eff}$ on the final nucleon fluxes is shown in Fig. 7, where unnormalized fluxes of the initial and final protons as well as of neutrons escaping from the source before decaying are shown for the same cases as above. The main effect of diffusion on the final proton spectrum is a reduction of the flux in the energy window between $E_{\rm th}$ and E_L. This reduction is proportional to the increase of the effective interaction depth as long as $\tau_{\rm eff} \lesssim 1$. Thus, the dependence of the proton flux can be deduced directly from the behavior of $\tau_{\rm eff}$, which in turn depends on $R_{\rm eff}$.

In the case of neutrons, changes in the flux are also tightly correlated to variations of $R_{\rm eff}$. The increase of $\tau_{\rm eff}$ for protons implies more scatterings and therefore a
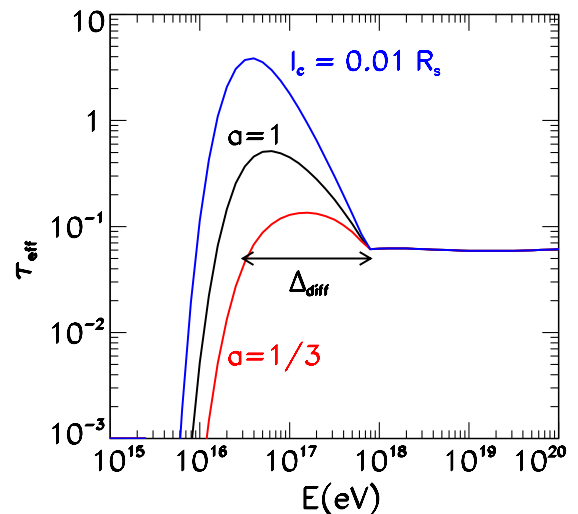

FIG. 6 (color online). Effective interaction depth $\tau_{\rm eff}$ for the same source parameters as in Fig. 5.
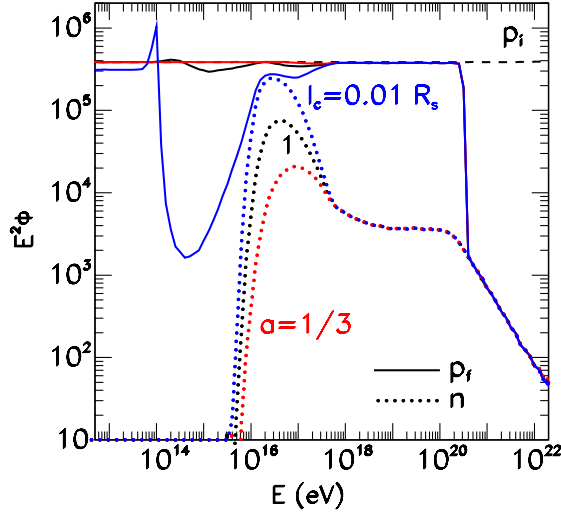
FIG. 7 (color online). Unnormalized fluxes of initial protons (dashed), neutrons escaping the source before decaying (dotted), and the cosmic ray flux (sum of escaped protons plus protons from neutron decays, solid line) for the same source parameters as in Fig. 5.

larger number of produced neutrons. Since the interaction depth of neutrons is not affected by diffusion, all neutrons escape from the source before decaying, if the source is transparent. This increased production of neutrons due to the diffusion of protons stops at E_L. At intermediate energies there is a flat plateau of the neutron flux. Its slope is approximately the one of the initial proton flux, only slightly modified by the weak energy dependence of the $p\gamma$ cross section.

B. High energy protons and energy losses

At high energies, when the synchrotron loss length l_{syn} becomes smaller than the size of the source R_s, cf. Fig. 5, the proton flux is strongly suppressed. For earlier discussions of the impact of synchrotron [27], but also of other energy losses, on the resulting cosmic ray spectra, see e.g. Ref. [28].

From Eq. (7), this limiting energy[3] follows as

$$E_{syn} = \frac{3}{2\alpha}\left(\frac{B_{cr}}{B}\right)^2 \frac{1}{R_s}. \qquad (16)$$

Above this energy, the main component of the nucleon flux is neutrons produced in scatterings. The energy losses of protons lead to a steepening of the proton flux and therefore also of the neutron flux. This steepening can be estimated for a transparent source by noting that the energy of protons decreases with distance l in the classical limit as

---

[3]The limiting energy E_{syn} should be distinguished from the maximal acceleration energy E_{max}, defined by setting synchrotron energy losses equal to the energy gain in an electromagnetic field, $E_{max} = [(3m^4)/(2\alpha^3 B)]^{1/2}$. The latter is evaluated for the magnetic field in the acceleration region.

$$y = \frac{E_f}{E_i} = \frac{1}{1 + b_0 E_i l}, \qquad (17)$$

where $b_0 \equiv W_{cl}/E^2 = (2/3)\alpha(B/B_{cr})^2$. Hence, the energy of a proton that interacts and produces a neutron is reduced on average by the factor $\langle y \rangle = \int_0^R dl\, y \propto 1/E_i$ (neglecting logarithmic corrections). Therefore the exponent of the neutron spectrum is increased by one, $\alpha_n = \alpha_g + 1$, compared to the generation spectrum of protons.

Perhaps surprisingly, the final proton flux of a magnetized source is not just a broken power law, with $\alpha = \alpha_g$ below and $\alpha = \alpha_g + 1$ above E_{syn}. Instead, there is additionally a step in the flux at E_{syn}, where, e.g., the flux shown in Fig. 7 decreases suddenly by 2 orders of magnitude. The reason for this step is that the final proton flux at $E < E_{syn}$ consists both of escaping "direct" protons and of the ones produced in decays of escaping neutrons, whereas at $E > E_{syn}$ only the second contribution is significant. The difference in the relative size of the final cosmic ray flux at $E > E_{syn}$ and $E < E_{syn}$ corresponds to the ratio R of the neutron and proton flux in the plateau region, here at 10^{18} eV–10^{20} eV. It can be estimated for transparent sources as $R_0 \sim \tau_0 \times BR(p \to n) \times (1 - \langle y(\alpha_g) \rangle)$, where $1 - \langle y(\alpha_g) \rangle$ is the spectrally averaged energy transfer from protons to neutrons. If the interaction depth is large, protons produce neutrons before losing too much energy due to synchrotron losses. Therefore, the step at E_{syn}, where the cosmic ray flux leaving the source changes from neutron to proton dominated, increases for smaller τ_0. This step in the emitted cosmic ray flux at E_{syn} acts in the case of rather transparent sources, $\tau_0 \ll 1$, effectively as the maximal energy of the source. The distribution of maximal magnetic field strengths in different sources and the resulting distribution of maximal energies dn/dE_{max} leads thus to a steepening of the observed diffuse cosmic ray flux and may thereby reconcile the observed steep spectrum $\alpha_g \approx 2.6$ with the expectation $\alpha_g \approx 2.0$–2.2 from Fermi shock acceleration [29].

C. Dependence on the magnetic field strength

Let us discuss now the impact of the magnetic field strength on the nucleon flux. Increasing B has two main consequences: On the one hand, the energy range Δ_{diff} with diffusion increases, because $E_L \propto B$. On the other hand, synchrotron radiation losses become important for lower energies, as $E_{syn} \propto 1/B^2$. Thus, an increase of the magnetic field strength widens the energy range Δ_{diff} with diffusion until $E_L = E_{syn}$. Increasing B even further, Δ_{diff} narrows again and synchrotron losses influence finally the whole spectrum. This dependence is clearly illustrated by Fig. 8, where the nucleon fluxes for a source with a temperature of $T = 10^4$ K, size $R_s = 2.5 \times 10^{13}$ cm ($\tau_0 = 0.1$), and three different magnetic fields $B = 10$ G (black), 100 G (red), and 10^4 G (blue) are shown. In the last case, the cosmic ray
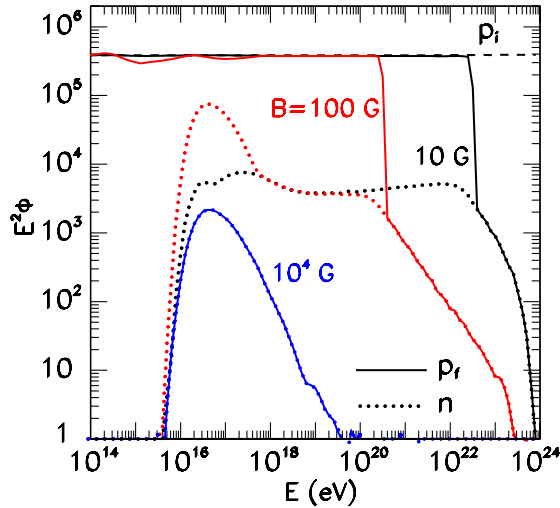
FIG. 8 (color online). Unnormalized fluxes of initial protons (dashed), neutrons escaping the source before decaying (dotted), and the cosmic ray flux (sum of escaped protons plus protons from neutron decays, solid line) for a source with a temperature of $T = 10^4$ K, size $R_s = 2.5 \times 10^{13}$ cm ($\tau_0 = 0.1$), and magnetic field $B = 10$ G (black), 100 G (red), and 10^4 G (blue).
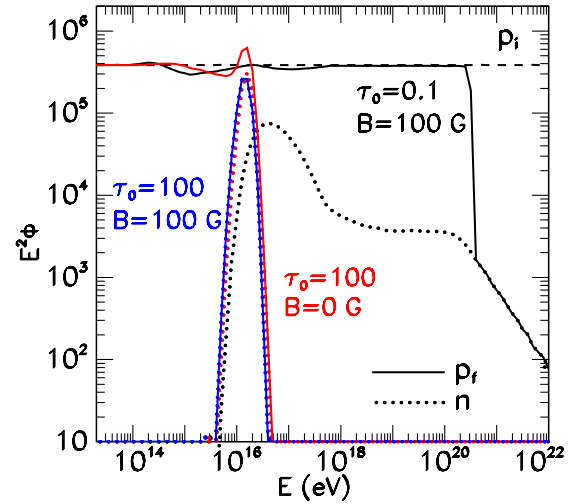

FIG. 9 (color online). Unnormalized fluxes of initial protons (dashed), neutrons escaping the source before decaying (dotted), and the cosmic ray flux (sum of escaped protons plus protons from neutron decays, solid line) for a source with a temperature of $T = 10^4$ K, size $R_s = 2.5 \times 10^{13}$ cm ($\tau_0 = 0.1$), and magnetic field $B = 10^2$ G (black), $R_s = 2.5 \times 10^{16}$ cm ($\tau_0 = 10^2$) and $B = 10^{-5}$ G (red), and $R_s = 2.5 \times 10^{16}$ cm ($\tau_0 = 10^2$) and $B = 10^2$ G (blue).

flux is strongly suppressed and the main part of the source luminosity is damped into electromagnetic cascades.

D. Dependence on the interaction depth

Let us next consider the consequences of the magnetic field strength on the nucleon flux from a thick source, $\tau_0 \gtrsim 1$. As discussed in Ref. [9], the characteristic property of a thick source is the strong suppression of the nucleon flux at energies above the photopion production threshold due to multiple scattering. For the unmagnetized, thick source in Fig. 9, the final proton flux is cut off at $E_{\text{th}} \approx 10^{16}$ eV followed by a small bump, while at lower energies the proton flux is hardly affected as long as R_s is smaller than the typical length scale for e^+e^- pair production, see Fig. 5. The neutron flux is narrowly peaked around E_{th}, where the neutron interaction length decreases and the escape probability increases.

The consequences of magnetic fields in a thick source are twofold. At high energies, there is a competition between multiple scattering and synchrotron radiation as the main energy loss process. Analogous to Eq. (16), we define as critical energy

$$E_{\text{syn}} = \frac{3}{2\alpha}\left(\frac{B_{\text{cr}}}{B}\right)^2 \frac{1}{l_{\text{int}}}.$$ (18)

While both processes lead to a strong suppression of the nucleon flux at high energies, only the latter transfers the energy to neutrinos. In contrast, magnetic fields influence not only the neutrino but also the cosmic ray flux at low energies. Since diffusion increases the effective size R_{eff} of the source below E_L, synchrotron and e^+e^- pair production losses can suppress the proton flux even below the

pion-production threshold. As a result, the final cosmic ray flux may consist only of neutrons which escape near E_{th}. As an example for such a situation, we show the proton and neutron flux from a source with $B = 100$ G and $\tau_0 = 100$ in Fig. 9 that is narrowly concentrated around the threshold energy.

IV. NEUTRINO YIELDS

In order to analyze the effect of the magnetic fields of the source on the neutrino spectrum, we study now the neutrino yield of a single source. The neutrino yield $Y_\nu(E)$, i.e. the ratio $Y_\nu(E) = \phi_\nu(E)/(p_{\text{int}}\phi_p(E))$ of the emitted neutrino flux ϕ_ν and the product of the interaction probability $p_{\text{int}} = 1 - \exp(-\tau_0)$ and the injected proton flux ϕ_p, represents the number of neutrinos produced per injected interacting proton with the same energy.[4]

A. General characteristics

The dependence of the neutrino yields on the source parameters can be deduced from the corresponding behavior of secondary mesons in the source. Therefore we complement the typical length scales shown in Fig. 5 for protons with those for mesons in Fig. 10. We have added the typical length of inverse Compton scattering for muons as well as the decay lengths $l_{\text{dec}} = \gamma l_{1/2}$ of mesons and muons.

---

[4]Note that this definition differs from the standard one, $Y_\nu(E) = \phi_\nu(E)/(\tau_0 \phi_p(E))$, that was also used in Ref. [9].
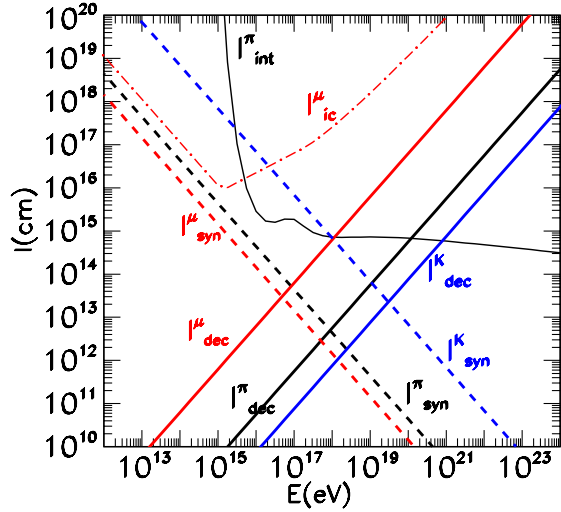
FIG. 10 (color online). Decay lengths (thick solid) and the typical length scale of synchrotron losses (dashed) for charged pions (black), charged kaons (blue), and muons (red) for a source with temperature $T = 10^4$ K, size $R_s = 2.5 \times 10^{13}$ cm ($\tau_0 = 0.1$), and magnetic field $B = 10^2$ G. The interaction length for pions (thin solid) as well as the typical length of inverse Compton scattering for muons (dot-dashed) have been included.

The most important difference with respect to a source with negligible magnetic fields is the appearance of a length scale, $l_{\rm syn} \propto 1/E$, which decreases with energy (as long as $\chi \ll 1$). Hence, the synchrotron length becomes for a magnetized source at high enough energies always the smallest length scale, and in turn meson decays and the neutrino flux will be suppressed.

We modify Eq. (16) to take into account possible meson and muon decays, defining

$$E_{i,\rm syn} = \frac{3}{2\alpha}\left(\frac{B_{i,\rm cr}}{B}\right)^2 \frac{1}{R_s} \quad \text{for } f_i(B, R_s) \lesssim 1, (19a)$$

$$E_{i,\rm syn} = \left(\frac{3}{2\alpha}\left(\frac{B_{i,\rm cr}}{B}\right)^2 \frac{m_i}{l_{i,1/2}}\right)^{1/2} \quad \text{for } f_i(B, R_s) \gtrsim 1, (19b)$$

where the functions $f_i(B, R_s)$ are defined as

$$f_i(B, R_s) = \frac{2\alpha}{3}\left(\frac{B}{B_{i,\rm cr}}\right)^2 \frac{R_s^2 m_i}{l_{i,1/2}}. \tag{20}$$

The first expression represents the condition $l_{\rm syn}(E_{\rm syn}) = R_s$. At energies above $E_{\rm syn}$, charged mesons lose energy by synchrotron radiation. Mesons with energies between $R_s l_{1/2}/m$ and $E_{\rm syn}$ escape from the source before decaying. At energies smaller than $R_s l_{1/2}/m$ mesons decay inside the source. The second expression corresponds to $l_{\rm syn}(E_{\rm syn}) = l_{\rm dec}(E_{\rm syn})$. In this situation mesons with energies below $E_{\rm syn}$ decay always within the source.

For given source parameters, the limiting energy $E_{\rm syn}$ above which synchrotron losses become crucial increases with mass and decreases with the decay length of a particle.

As a consequence, muons and pions are affected already at much lower energies than kaons and protons [11,12].

In Fig. 11, we show how different reactions contributing to the neutrino yield are affected by magnetic fields. The increase of the number of $p\gamma$ interactions at low energies by diffusion has two main consequences for the neutrino production: First, a larger number of neutrons is produced, which will freely escape in the case of a transparent source. Second, the number of generated pions increases. The former leads to a bump of $\bar{\nu}_e$ around the energy $\approx 10^{-3} E_{\rm th}$. The latter produces another bump of neutrinos produced by pion decay roughly at $E_{\rm th}$. These two characteristics can be clearly observed in Fig. 11.

The high energy end of the spectrum is mainly influenced by synchrotron losses. The relative importance of different channels to the total neutrino yield is determined by the relative size of the synchrotron energy, $E_{\rm syn}^\mu < E_{\rm syn}^\pi < E_{\rm syn}^K$, cf. Fig. 10. Therefore, between the threshold energy for pion production and $E_{\rm syn}^\pi$ pion decays are the most important contribution to the neutrino yield. At slightly higher energies, between $E_{\rm syn}^\pi$ and $E_{\rm syn}^K$, neutrinos from the decay of charged kaons dominate. For the source considered in Fig. 10, all neutrinos are produced in the decay of K_L^0's at the highest energies, as they are not directly affected by synchrotron losses. As discussed for neutrons, synchrotron losses of protons lead however to a steepening of the K_L^0 spectrum and in turn also to a steeper neutrino spectrum from these decays. We note that, in contrast to K_L^0, the K_S^0 contribution is suppressed roughly at $E_{\rm syn}^\pi$. The reason for this is that the main decay channel of K_S^0's giving rise to neutrinos is $\pi^+\pi^-$.
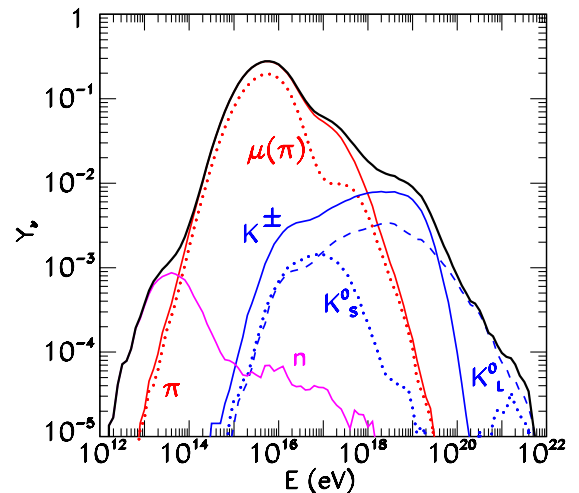

FIG. 11 (color online). Neutrino yield Y_ν from the decay of charged pions (solid red), charged kaons (solid blue), K_L^0 (dashed blue), K_S^0 (dotted blue), and neutrons (solid magenta). In the case of pions we also show the fraction of neutrinos produced by the muons generated in the pion decay (dotted red). The same source parameters as in Fig. 10 have been assumed.

Beside the neutron and pion neutrino bump at low energies and the suppression at high energies due to synchrotron losses, there is a third characteristic feature at intermediate energies: muon damping in the energy range between E_{syn}^{μ} and E_{syn}^{π} [13]. While the synchrotron lengths l_{syn} of pions and muons are comparable, their decay lengths l_{dec} differ by more than 2 orders of magnitude. As a consequence, muons with an energy between E_{syn}^{μ} and E_{syn}^{π} created from pion decay cannot further decay but lose energy by synchrotron radiation. Hence, most neutrinos in that energy range are ν_{μ} produced directly in pion decays.

In order to estimate the energy range where the effect of muon damping is potentially strong, we define the muon damping width Δ_{μ} analogous to Δ_{diff} as

$$\Delta_{\mu} \equiv \log(E_{\text{syn}}^{\pi}) - \log(E_{\text{syn}}^{\mu}). \qquad (21)$$

The muon damping width depends on the source parameters R_s and B only indirectly via the choice between (19a) and (19b). Let us first consider a source such that $f_{\mu}(B, R_s) \gtrsim 1$, i.e. $(B/\text{G})(R_s/\text{cm}) \gtrsim 3 \times 10^{15}$. In this case, all muons produced in pion decay with energies between E_{syn}^{μ} and E_{syn}^{π} are generated inside the source and therefore are affected by the synchrotron losses. Hence, muons are completely damped within this energy range. The muon damping width is maximal and equals $\Delta_{\mu} \approx 0.5 \times \log[(m_{\pi}/m_{\mu})^5 (l_{\mu}/l_{\pi})] \approx 1.3$. If $f_{\mu}(B, R_s) \lesssim 1$, some of the muons produced can escape from the source before decaying. Let us now consider a source such that $f_{\pi}(B, R_s) \lesssim 1$, i.e. $(B/\text{G})(R_s/\text{cm}) \ll 5 \times 10^{14}$. In this case, pions with energies between $R_s l_{\pi,0}/m_{\pi}$ and E_{syn}^{π} decay outside the source, and then there is no muon damping. The numerical values used in Fig. 11, $(B/\text{G}) \times (R_s/\text{cm}) = 2.5 \times 10^{15}$, correspond to partial muon damping, as can be observed in the figure.

A similar damping effect occurs for muons from charged kaon decays. Now the numerical value of the width, Eq. (21), is larger. However, the effect is not as strong as in the case of pions, because the energy range where kaons dominate is narrower and also their number of decay channels is larger.

B. Dependence on the properties of the source

We now analyze how the general characteristics previously discussed depend on the different properties of the source.

1. Diffusion regime

In Fig. 12, we present the neutrino yields for sources with different diffusion conditions, choosing those already used in Sec. III A. As previously discussed, diffusion generates two bumps, one from neutrinos created by neutron decay at very low energies, and another one of neutrinos produced in the decay of charged pions at $E \approx E_{\text{th}}$. The intensity of these peaks is directly related to the character-
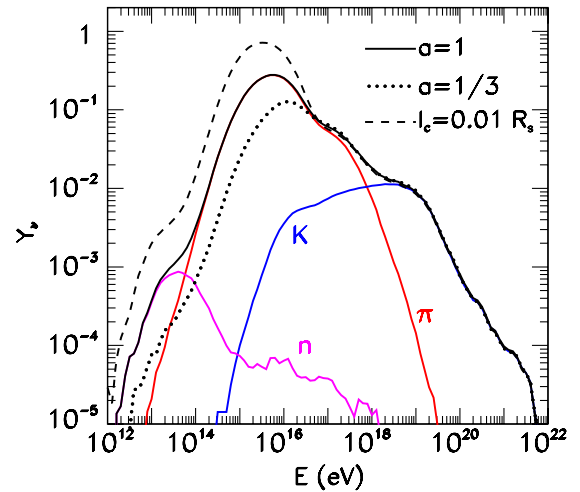

FIG. 12 (color online). Neutrino yield Y_{ν} produced in sources with the same parameters considered in Fig. 5. The different reactions giving rise to Y_{ν} in the case of the source with Bohm diffusion ($a = 1$) and $l_c = R_s$ are also shown.

istics of diffusion, in particular, to τ_{eff}. A comparison of the yields with Figs. 5 and 6 confirms the expected correlation between the height of the neutrino bumps at low energies and the effective interaction depth at the correct energy range. Also, the different diffusion regimes do lead to the same neutrino yield at high energies.

2. Magnetic field strength

In Fig. 13, we show the dependence of the neutrino yield on the magnetic field strength. As discussed in Sec. III C
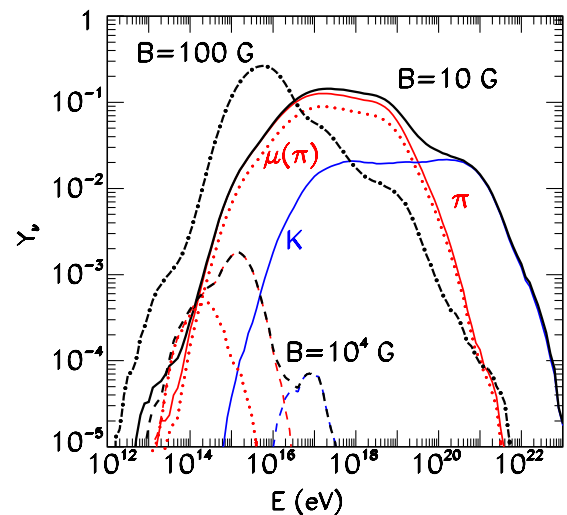

FIG. 13 (color online). Neutrino yield Y_{ν} produced in sources with the same parameters assumed in Fig. 8. The different contributions to Y_{ν} in the case of the source with $B = 10$ G and $B = 10^4$ G are also shown. The fraction of neutrinos produced by the muons generated in the pion decay (dotted red) is also indicated.

two main effects are expected. At low energies, the larger the magnetic field strength the more intense is diffusion and hence the interaction depth. This translates into an increase of the neutrino yield at low energies, and, in particular, into a higher bump of the contribution to the neutrino yield coming from pion and neutron decay. This can be easily confirmed by comparing the two sources with 10 and 100 G in Fig. 13.

The second consequence of a larger magnetic field strength is a more severe suppression of the neutrino yield at high energies due to synchrotron radiation. Since the energy at which synchrotron losses become important is proportional to $1/B^2$, the suppression of the neutrino yield starts earlier in the source with 10^2 G than in the one with 10 G, while for $B = 10^4$ G the neutrino yield is suppressed in the whole energy range, cf. Fig. 13.

The value of the magnetic field strength also affects muon damping, enhancing the damping for a stronger field. For the case of a source with 10 G shown in Fig. 13, the product $(B/G)(R_s/cm) = 2.5 \times 10^{14} < 5 \times 10^{14}$. Therefore most pions decay outside the source and thus muons are not affected by the magnetic field. If the magnetic field is increased to 10^4 G, then $(B/G)(R_s/cm) = 2.5 \times 10^{17} \gg 3 \times 10^{15}$ and complete muon damping occurs.

3. Interaction depth

We analyze now the influence of the interaction depth τ_0 on a magnetized neutrino source. Figure 14 shows the different contributions to the neutrino yield for a source with the same parameters as the one in Fig. 11, but for $\tau_0 = 100$ instead of $\tau_0 = 0.1$.
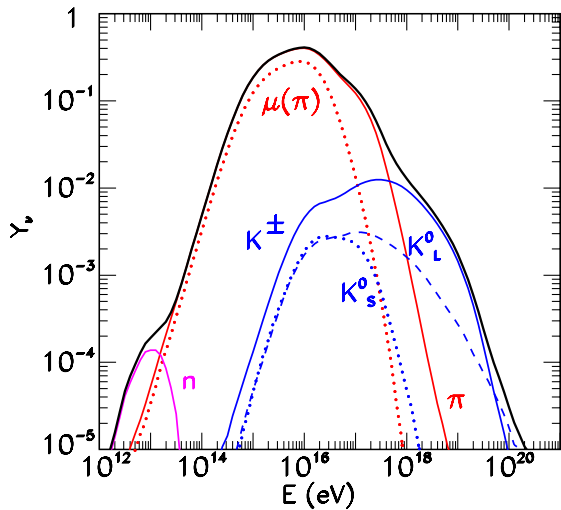

FIG. 14 (color online). Neutrino yield Y_ν from the decay of charged pions (solid red), charged kaons (solid blue), K_L^0 (dashed blue), K_L^0 (dotted blue), neutrons (solid magenta), and charm mesons (solid green) for a source with temperature $T = 10^4$ K, size $R_s = 2.5 \times 10^{16}$ cm ($\tau_0 = 10^2$), and magnetic field $B = 10^2$ G. The fraction of neutrinos produced by muons from the pion decay (dotted red) is also indicated.

At low energies, the narrowly peaked spectrum of neutrons leaving a thick source is responsible for the absence of the high energy tail of the neutrinos produced in neutron decay. The number of neutrinos from pion decay in this range is not influenced strongly, because multiple scattering occurs in both cases either because of large τ_{eff} or large τ_0.

At high energies there are some differences. In the case of thin sources, the most important contribution to the neutrino yield comes from the decay of neutral kaons, see Fig. 11, since they are not directly affected by synchrotron losses. In the case of sufficiently thick sources, also most neutral kaons interact with the photons and thus the neutrino production from these decays is suppressed, see Fig. 9. In Ref. [9], it was shown that neutrinos from decays of charmed mesons became the dominant contribution at the highest energies for a source with $\tau_0 \gg 1$. In principle, the same holds in the case of sources with magnetic fields. However, synchrotron losses above $E \gtrsim E_{syn}$ may significantly suppress the proton flux and thus also the production of charmed mesons produced. For the source considered in Fig. 9, the contribution from charm decays is negligible.

In the case of charged mesons and muons, it is possible to redefine the energy at which synchrotron radiation becomes the dominant energy loss process substituting R_s by l_{int} into Eq. (19). If $f_\pi(B, l_{int}) \lesssim 1$ then pions with energies between $l_{int} m_\pi/l_0^\pi$ and E_{syn}^π scatter before decaying. If $f_\pi(B, l_{int}) \gtrsim 1$ then pions decay inside the source whereas muons with energies higher than E_{syn}^μ will suffer energy losses by synchrotron radiation before decaying. Therefore the condition for having muon damping in a thick source can be written as $f_\pi(B, l_{int}) \gtrsim 1$ or equivalently $(B/G) \times (l_{int}/cm) \gtrsim 5 \times 10^{14}$, which clearly satisfied by the source considered in Fig. 9.

V. FLAVOR DEPENDENCE OF NEUTRINO YIELDS

Both neutrino telescopes and extensive air-shower experiments have some flavor discrimination possibilities. The case of neutrino telescopes was discussed for the example of ICECUBE in detail in Ref. [30], for air-shower experiments see Ref. [31]. The main observable for the neutrino flavor composition is the ratio of track to shower events in a neutrino telescope, $R_\mu = \phi_\mu/(\phi_e + \phi_\tau)$, while only in a very small energy range all flavors can be distinguished. Additionally, extensive air-shower experiments are sensitive to the fraction of tau events in all horizontal neutrino events, $R_\tau = \phi_\tau/(\phi_e + \phi_\mu)$, in a small energy window around 10^{18} eV.

In spite of these flavor discrimination possibilities, the potential of high energy neutrino observations for mixing parameter studies has been realized only recently [32], for some follow-up studies see [33]. One of the main reasons for this missing interest has been the prejudice that the maximal mu-tau mixing together with the expected flavor

ratio $\phi(\nu_e){:}\phi(\nu_\mu){:}\phi(\nu_\tau) = 1{:}2{:}0$ from pion decay prevents oscillation studies with high energy neutrinos. The key observation of Refs. [32] was that there exist however several examples of neutrino sources where at least in some energy range significant deviations from this canonical flavor ratio from pion decay can be expected. Our results indicate that deviations from the canonical flavor ratio $\phi(\nu_e){:}\phi(\nu_\mu){:}\phi(\nu_\tau) = 1{:}2{:}0$ are much more common than previously thought. In the following, we will show that magnetized sources are characterized by a strongly energy-dependent flavor ratio and thus the flavor ration encodes nontrivial information.

A. Energy dependence of the neutrino flavor ratio at the source

We start with an analysis of the expected neutrino flavor ratio $R^0 \equiv Y_{\nu_\mu}/Y_{\nu_e}$ at the source. In Fig. 15 we show the flavor ratio at the source R_0 for four different sources with $T = 10^4$: $B = 0$ G, and $R_s = 2.5 \times 10^{13}$ cm ($\tau_0 = 0.1$) (black), $B = 0$ G, and $R_s = 2.5 \times 10^{16}$ cm ($\tau_0 = 100$) (magenta), $B = 100$ G, and $R_s = 2.5 \times 10^{13}$ cm ($\tau_0 = 0.1$) (blue), $B = 100$ G and $R_s = 2.5 \times 10^{16}$ cm ($\tau_0 = 10^2$) (red). In the case of a transparent source with negligible magnetic field strength the flavor ratio basically does not depend on energy. However, the presence of magnetic fields as well as large interaction depths can result in complicated structures of the flavor ratio. The different bumps arising at different energies are tightly related to
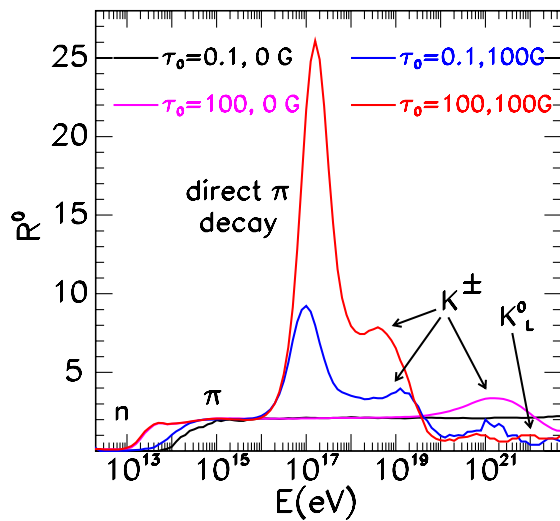

FIG. 15 (color online). Flavor ratio R^0 of the neutrinos produced in a source at $T = 10^4$, $B = 0$ G, and $R_s = 2.5 \times 10^{13}$ cm ($\tau_0 = 0.1$) (black), $B = 0$ G, and $R_s = 2.5 \times 10^{16}$ cm ($\tau_0 = 100$) (magenta), $B = 100$ G, and $R_s = 2.5 \times 10^{13}$ cm ($\tau_0 = 0.1$) (blue), and $R_s = 2.5 \times 10^{16}$ cm ($\tau_0 = 100$) (red) before they oscillate. The main reactions giving rise to the neutrino signal are also shown. The neutrinos produced in the muon damping are indicated as direct π decay.

the different processes taking place in the formation of the neutrino flux.

Let us analyze these structures for each case. The flavor ratio R_0 of all sources is zero below the pion-production threshold as most neutrinos are $\bar{\nu}_e$ produced in neutron decay. Right after the energy threshold for pion production, R_0 becomes two, typical for π decay. At higher energies the behavior of the flavor ratio strongly depends on the characteristics of the source. Let us first summarize the two cases with negligible magnetic fields. If the source is transparent, then R_0 remains constant, $R_0 \approx 2$. Thick sources show, though, a bump exactly at the energy at which there is a crossover between pion and charged kaon neutrino dominance, namely, where $l_{\text{int}}^\pi(E) = l_{\text{dec}}^\pi(E)$. At higher energies, the flavor ratio tends to one, when all neutrinos come from the decay of charmed mesons, see Ref. [9].

In the case that sources have non-negligible magnetic fields, the energy dependence of the flavor ratio becomes more complex. The main feature is the presence of a strong peak arising between E_{syn}^μ and E_{syn}^π, in this case around $E \approx 10^{17}$ eV. This clearly reflects the energy window where muon damping occurs. In this case the only neutrinos produced are the ν_μ generated directly from pion decay. The accompanying muons lose energy instead of decaying, therefore no electron neutrinos are produced. As a consequence R_0 increases, the final value depending on the strength of the muon damping. By comparing Figs. 11 and 14, one expects a stronger effect for a thick source, as can be observed in the figure. At higher energies there is an energy range where neutrinos are produced in the decay of charged kaons, analogously to the case of thick source with negligible magnetic fields. In contrast to this case, though, the energy range of charged kaon dominance happens at lower energies. The reason is that the crossover between pions and charged kaon neutrinos takes place at E_{syn}^π, which, for the sources considered in Fig. 15, is smaller than the energy where $l_{\text{int}}^\pi(E) = l_{\text{dec}}^\pi(E)$. The different height of the bump observed in the transparent and thick sources is related to the muon damping happening also for the charged kaons in the latter case. Finally, at the highest energies one expects a tendency toward one, either because these neutrinos are produced via $K_L^0 \to \pi + e + \nu_e$, as in the figure, or because they come from the decay of charmed mesons.

We conclude that there is a direct relationship between the energy dependence of the flavor ratio R_0 and the different processes contributing to the neutrino yield, that may be used to deduce the intrinsic characteristics of the source.

B. Effect of neutrino oscillations

The neutrino spectra at the source discussed in the preceding subsection are modulated by oscillations. Therefore the expected flavor ratios R_i at the Earth are different from the original ratios R_i^0 at the source.

The neutrino fluxes arriving at the detector, ϕ_α^D, can be written in terms of the initial fluxes ϕ_α and the conversion probabilities $P_{\alpha\beta}$,

$$\phi_\alpha^D = \sum_\beta P_{\alpha\beta}\phi_\beta = P_{\alpha e}\phi_e + P_{\alpha\mu}\phi_\mu. \qquad (22)$$

Since the interference terms sensitive to the mass splittings Δm^2's do not contribute, the conversion probabilities are simply

$$P_{\alpha\beta} = \delta_{\alpha\beta} - 2\sum_{j>k}\Re(U_{\beta j}^\star U_{\beta k}U_{\alpha j}U_{\alpha k}^\star), \qquad (23)$$

where U is the neutrino mixing matrix and Greek (Latin) letters are used as flavor (mass) indices.

In Fig. 16, we show the expected flavor ratio R_μ at the detector for a source with $T = 10^4$, $B = 10^2$ G, and $R_s = 2.5 \times 10^{16}$ cm ($\tau_0 = 10^2$), as a solid, red line for the best-fit point of the neutrino mixing parameters, $\sin^2\vartheta_{12} = 0.3$, $\sin^2\vartheta_{23} = 0.5$ and $\vartheta_{13} = 0$ [34]. Various bands show the range of R_μ allowed if the mixing parameters are varied within their 95% C.L., while the unconstrained CP phase δ_{CP} is varied in the whole possible range, $\delta_{CP} \in [0:\pi]$. Dominant uncertainty for the prediction of R_μ is the value of ϑ_{23}.

The main effect of neutrino oscillations is to smear out the structures of the initial flavor ratio R_0. Nevertheless, the remaining energy dependence still allows for an identification of the different regimes described in Sec. VA. On the other hand, its dependence on the neutrino mixing
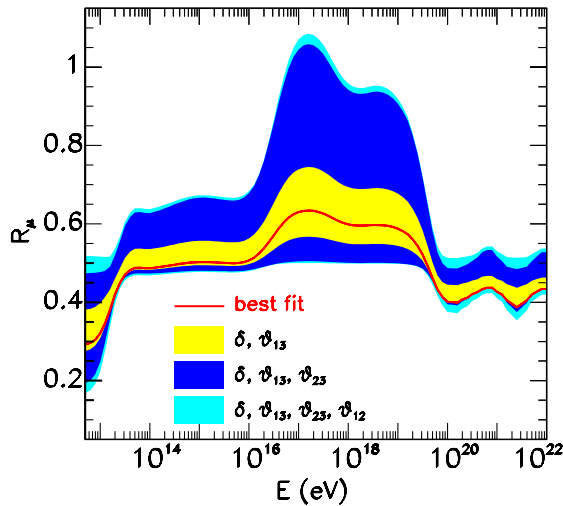

FIG. 16 (color online).   Flavor ratio R_μ at the Earth for a source with $T = 10^4$, $B = 10^2$ G, and $R_s = 2.5 \times 10^{16}$ cm ($\tau_0 = 10^2$). The solid red line (gray) corresponds to the best-fit point of the neutrino mixing parameters, $\sin^2\vartheta_{12} = 0.3$, $\sin^2\vartheta_{23} = 0.5$, and $\vartheta_{13} = 0$. In the colored areas mixing angles within 95% C.L. and a possible nonzero value of δ_{CP} have been considered: ϑ_{13} and δ_{CP} in yellow (very light gray), plus ϑ_{23} in blue (dark gray), and ϑ_{12} in green (light gray).

parameters offers the additional possibility to obtain information on neutrino properties.

VI. SUMMARY AND CONCLUSIONS

We have calculated in this work the yield of high energy neutrinos produced in astrophysical sources for arbitrary interaction depths τ_0 and magnetic field strengths B. Diffusion of protons increases their path length and hence also the effective interaction depth $\tau_{\rm eff}$. Therefore magnetized sources can lose their transparency, while the neutrino fluxes can be increased in this energy range. Sources with $\tau_{\rm eff} \gtrsim 1$ require to account for multiple scatterings and for secondary meson-photon interactions. For the latter task, we have extended the SOPHIA model in a self-consistent way.

Magnetic fields present in the surrounding of the acceleration region lead not only to diffusion of charged particles, but induce also synchrotron radiation as the most important energy loss process. Synchrotron losses result in a strong suppression of the cosmic ray flux and hence also of the neutrino flux at high energies, $E \gtrsim E_{\rm syn}$.

The cosmic ray upper bound of Refs. [7,8] relies on, among others, the assumption that the cosmic ray (without propagation effects) and the neutrino flux have the same spectral shape. The strong deviation of the escaping cosmic ray and neutrino fluxes from the injected power law found by us therefore undermines the basis of this bound even for transparent sources.

Since the relative importance of the various channels contributing to the neutrino yields changes strongly as a function of the energy, large variations exist in the neutrino flavor composition emitted by a magnetized source. These variations are for magnetized sources even stronger than those found previously for sources with negligible magnetic fields in Ref. [9]. In particular, we have examined two specific examples discussed earlier in the literature, namely, the cases where the neutrino spectrum is dominated by kaon decays [11,12] or influenced by the damping of muons produced in pion decays [13]. In addition, we have pointed out the possible existence of an analogous muon damping in the case of charged kaon decay at high energies. We have analyzed the conditions required for a source to present these features in the neutrino yield. In particular, we have found that muon damping and kaon dominance may influence the neutrino yields in the same source, but in different energy ranges.

The application of our simulation to concrete astrophysical models and the calculation of diffuse neutrino fluxes will be performed in paper III of this series [16].

[1] V. S. Beresinsky and G. T. Zatsepin, Phys. Lett. **28B**, 423 (1969); Sov. J. Nucl. Phys. **11**, 111 (1970); for recent works, see e.g. D. V. Semikoz and G. Sigl, J. Cosmol. Astropart. Phys. 04 (2004) 003.

[2] V. Berezinsky, Proceedings of Neutrino 1977, Elbros; D. Eichler, Astrophys. J. **232**, 106 (1979).

[3] F. W. Stecker, C. Done, M. H. Salamon, and P. Sommers, Phys. Rev. Lett. **66**, 2697 (1991); **69**, 2738(E) (1992); see also F. W. Stecker, Phys. Rev. D **72**, 107301 (2005); A. P. Szabo and R. J. Protheroe, Astropart. Phys. **2**, 375 (1994).

[4] K. Mannheim, Astropart. Phys. **3**, 295 (1995); A. M. Atoyan and C. D. Dermer, Astrophys. J. **586**, 79 (2003); New Astron. Rev. **48**, 381 (2004).

[5] E. Waxman and J. N. Bahcall, Phys. Rev. Lett. **78**, 2292 (1997); M. Vietri, Phys. Rev. Lett. **80**, 3690 (1998).

[6] V. S. Berezinsky and A. Yu. Smirnov, Astrophys. Space Sci. **32**, 461 (1975); V. S. Berezinsky, in Proceedings of "Neutrino-77", Baksan, USSR, edited by M. A. Markov, 1977, Vol. 1, p. 177.

[7] E. Waxman and J. N. Bahcall, Phys. Rev. D **59**, 023002 (1998).

[8] K. Mannheim, R. J. Protheroe, and J. P. Rachen, Phys. Rev. D **63**, 023003 (2000).

[9] M. Kachelrieß and R. Tomàs, Phys. Rev. D **74**, 063009 (2006).

[10] A. Mücke *et al.*, Comput. Phys. Commun. **124**, 290 (2000).

[11] S. Ando and J. F. Beacom, Phys. Rev. Lett. **95**, 061103 (2005).

[12] K. Asano and S. Nagataki, Astrophys. J. **640**, L9 (2006).

[13] T. Kashti and E. Waxman, Phys. Rev. Lett. **95**, 181101 (2005).

[14] V. S. Berezinsky, P. Blasi, and V. S. Ptuskin, Astrophys. J. **487**, 529 (1997); P. Blasi and S. Colafrancesco, Astropart. Phys. **12**, 169 (1999); S. Gabici and P. Blasi, Astrophys. J. **583**, 695 (2003); C. Rordorf, D. Grasso, and K. Dolag, Astropart. Phys. **22**, 167 (2004); D. De Marco, P. Blasi, P. Hansen, and T. Stanev, Phys. Rev. D **73**, 043004 (2006).

[15] V. S. Berezinsky and V. L. Ginzburg, Mon. Not. R. Astron. Soc. **194**, 3 (1981); V. S. Berezinsky and V. I. Dokuchaev, Astropart. Phys. **15**, 87 (2001); Astron. Astrophys. **454**, 401 (2006).

[16] M. Kachelrieß, S. Ostapchenko, and R. Tomàs, "High Energy Neutrino Yields from Astrophysical Sources III: Applications" (unpublished).

[17] C. Caso *et al.*, Eur. Phys. J. C **3**, 1 (1998).

[18] E. M. Levin and L. L. Frankfurt, JETP Lett. **2**, 65 (1965); H. J. Lipkin and F. Sheck, Phys. Rev. Lett. **16**, 71 (1966);

[19] J. J. J. Kokkedee and L. van Hove, Nuovo Cimento **42**, 711 (1966).

[19] P. D. B. Collins, *An Introduction to Regge Theory and High Energy Physics* (Cambridge University Press, Cambridge, England, 1977).

[20] A. Donnachie and P. V. Landshoff, Phys. Lett. B **296**, 227 (1992).

[21] T. Sjostrand, Int. J. Mod. Phys. A **3**, 751 (1988); Comput. Phys. Commun. **82**, 74 (1994).

[22] A. A. Sokolov and I. M. Ternov, *Radiation From Relativistic Electrons* (American Institute of Physics, New York, 1986).

[23] V. Berezinsky, A. Z. Gazizov, and S. I. Grigorieva, Phys. Rev. D **74**, 043005 (2006).

[24] G. R. Blumenthal and R. J. Gould, Rev. Mod. Phys. **42**, 237 (1970).

[25] R. Aloisio and V. Berezinsky, Astrophys. J. **612**, 900 (2004).

[26] For a discussion of the energy dependence of diffusion coefficients found in numerical simulations, see, e.g., F. Casse, M. Lemoine, and G. Pelletier, Phys. Rev. D **65**, 023002 (2001).

[27] G. A. Schott, *Electromagnetic Radiation* (Cambridge University Press, Cambridge, England, 1912); J. Schwinger, Phys. Rev. **75**, 1912 (1949). For a discussion of early applications of synchrotron radiation to astrophysics, see T. K. Breus, Ist.-Astronom. Iss. **26**, 88 (2001).

[28] R. J. Protheroe and T. Stanev, Astropart. Phys. **10**, 185 (1999); R. J. Protheroe, Astropart. Phys. **21**, 415 (2004).

[29] M. Kachelrieß and D. V. Semikoz, Phys. Lett. B **634**, 143 (2006).

[30] J. F. Beacom *et al.*, Phys. Rev. D **68**, 093005 (2003); **72**, 019901(E) (2005).

[31] J. G. Learned and S. Pakvasa, Astropart. Phys. **3**, 267 (1995); H. Athar, G. Parente, and E. Zas, Phys. Rev. D **62**, 093010 (2000).

[32] P. Bhattacharjee and N. Gupta, arXiv:hep-ph/0501191; P. D. Serpico and M. Kachelrieß, Phys. Rev. Lett. **94**, 211102 (2005); T. Kashti and E. Waxman, Phys. Rev. Lett. **95**, 181101 (2005).

[33] P. D. Serpico, Phys. Rev. D **73**, 047301 (2006); W. Winter, Phys. Rev. D **74**, 033015 (2006); W. Rodejohann, J. Cosmol. Astropart. Phys. 01, 029 (2007); O. Mena, I. Mocioiu, and S. Razzaque, Phys. Rev. D **75**, 063003 (2007); D. Meloni and T. Ohlsson, Phys. Rev. D **75**, 125017 (2007).

[34] M. Maltoni, T. Schwetz, M. A. Tortola, and J. W. F. Valle, New J. Phys. **6**, 122 (2004).